DOI: 10.61782/fa.2023.0224

forum acusticum 2023

OPTIMIZATION OF DAMPING PROPERTIES OF ACOUSTIC MEMS SHUTTER DEVICES

Dominik Mayrhofer[1*] **Manfred Kaltenbacher**[1]
[1] Institute of Fundamentals and Theory in Electrical Engineering, Graz University of Technology, Austria

ABSTRACT

Micro-Electro-Mechanical-Systems (MEMS) shutter devices are mostly known for optical applications as seen in the James Webb Space Telescope. Besides optics, shutter devices also find application in sound generation as for example Advanced Digital Sound Reconstruction as well as photo-acoustic gas sensors. In these applications, the damping as well as the sealing properties of the shutter is fundamental to the overall principle. A single unit cell of such an acoustic shutter device can be seen as a meta material which interacts with the acoustic wave. Due to the size of MEMS shutters, viscous effects as well as the back-coupling from the built up acoustic pressure has to be taken into account. In order to optimize such a device taking all necessary effects into account, a parameter study utilizing the linearized compressible flow equations formulated in an arbitrary Lagrangian-Eulerian (ALE) framework has been carried out. These equations are iteratively coupled to a standard mechanic computation as well as an artificial quasi-static mechanical computation governing the domain movement. Finally, based on the parameter study, an optimal point of operation with respect to certain hardware restrictions as for example the stiffness of the actuator as well as the necessary operating pressure has been evaluated.

Keywords: *MEMS, shutter, linearized compressible flow equations, ALE*

**Corresponding author*: *dominik.mayrhofer@tugraz.at.*

1. INTRODUCTION

In this paper, we present the optimization of damping properties for a Micro-Electro-Mechanical-Systems (MEMS) shutter used for ultrasound pulse-based principles. Due to the rise of MEMS applications in general, investigations of microstructures have drawn lots of research interest in the past 20 years [1–6]. The particular case of MEMS shutter devices ranges from biomedical to optical and recently acoustic applications [7–9]. For acoustic applications at the micro-scale special care has to be taken since viscous effects are often essential in the modeling process. Besides viscous effects, modeling shutter devices also requires taking the domain movement into account [9]. In this paper, we use the linearized compressible flow (LinFlow) equations in arbitrary Lagrangian-Eulerian (ALE) formulation to achieve this. The LinFlow equations are used in the literature, especially for applications where boundary layer-based approaches fail due to the complex geometry or where similar restrictions require the full set of equations [10, 11]. For the investigation of our device, we use the extended ansatz introduced in [12], where besides viscous acoustics on moving domains also fully coupled fluid-structure interaction is possible. For the actual optimization we perform a parameter study where we vary the pressure, the gap between the shutter and the stator, as well as the stiffness of the shutter mounting points. Based on the results of this study, we investigate the influence of different parameter choices and their effects on linearity, asymmetry, damping properties, and leakage behavior.

2. GOVERNING EQUATIONS

This section explains the mathematical framework used to optimize the shutter device. This ranges from viscous

acoustics in ALE formulation to the geometry deformation and the incorporation of the coupling.

2.1 Viscous acoustics

Since we focus on the damping properties of a shutter device, we use the linearized compressible flow equations in ALE formulation, which are given by

$$\frac{1}{\rho_0 c_0^2}\frac{\partial p}{\partial t} + \nabla \cdot \boldsymbol{v} - \frac{1}{\rho_0 c_0^2}\boldsymbol{v}_\mathrm{g} \cdot \nabla p = 0 \tag{1}$$

for the conservation of mass as well as

$$\rho_0 \frac{\partial \boldsymbol{v}}{\partial t} - \rho_0 \boldsymbol{v}_\mathrm{g} \cdot \nabla \boldsymbol{v} = \nabla \cdot [\boldsymbol{\sigma}] \tag{2}$$

for the conservation of momentum. Here, the fluid stress tensor $[\boldsymbol{\sigma}]$ is given by

$$[\boldsymbol{\sigma}] = -p\,[\boldsymbol{I}] + \mu_\mathrm{f}(\nabla \boldsymbol{v} + (\nabla \boldsymbol{v})^\intercal) - \frac{2}{3}\mu_\mathrm{f}(\nabla \cdot \boldsymbol{v})\,[\boldsymbol{I}]. \tag{3}$$

In these equations, ρ_0 denotes the mean density, c_0 the speed of sound, p the perturbed fluid pressure, and t the time. Furthermore, $\boldsymbol{v}$ stands for the perturbed fluid velocity and $\boldsymbol{v}_\mathrm{g}$ for the grid velocity. For the definition of the fluid stress tensor, we only consider Newtonian fluids and use the hypothesis of Stokes, which can represent the fluid stress tensor in terms of the pressure and the spatial derivatives of the velocity [13]. In Eqn. (3) $\boldsymbol{I}$ represents the identity matrix and μ_f the dynamic viscosity.

2.2 Geometry deformation

We use a quasi-static solution of an artificial mechanics problem for the geometry deformation. This artificial mechanics problem is solved together with the LinFlow-equations in an iterative approach and delivers the updated geometry and the grid velocity necessary for the domain movement. Although more expensive, the proposed approach has the advantage of being very flexible and robust, especially in combination with artificial location-dependent material parameters [14]. We introduce the so-called smooth PDE

$$-\nabla \cdot \left([\boldsymbol{C}] : \frac{1}{2}(\nabla \boldsymbol{u} + (\nabla \boldsymbol{u})^\intercal) \right) = 0, \tag{4}$$

which delivers the new coordinates directly, whereas the grid velocity is computed via a backward difference scheme of second order (BDF2 scheme) [14]. In Eqn. (4) $[\boldsymbol{C}]$ denotes the stiffness tensor and $\boldsymbol{u}$ the displacement vector of the artificial problem. The smooth PDE itself is only solved in domains where domain movement is incorporated, which is, in this case, only the region "LinFlow (moving)" as seen in Fig. 1.

2.3 Mechanics

To model the movement of the shutter itself, we use the classical mechanics PDE for small deformations given by

$$\rho_\mathrm{m}\frac{\partial^2 \boldsymbol{u}_\mathrm{m}}{\partial t^2} - \nabla \cdot \underbrace{\left([\boldsymbol{C}_\mathrm{m}] : \frac{1}{2}(\nabla \boldsymbol{u}_\mathrm{m} + (\nabla \boldsymbol{u}_\mathrm{m})^\intercal) \right)}_{[\boldsymbol{\sigma}_\mathrm{m}]} = \boldsymbol{f}_\mathrm{m}, \tag{5}$$

where $\boldsymbol{u}_\mathrm{m}$ denotes the displacement, ρ_m the density of the solid, $[\boldsymbol{C}_\mathrm{m}]$ the stiffness tensor, $[\boldsymbol{\sigma}_\mathrm{m}]$ the mechanical stress tensor and $\boldsymbol{f}_\mathrm{m}$ some volume force.

2.4 Acoustics

Finally, the acoustic wave equation in its pressure formulation is used to model the propagation of the acoustic waves in regions where neither viscous boundary layers nor domain movement is important. This reduces the number of unknowns and is a more computationally efficient approach. The acoustic wave equation (acoustics PDE) is given by

$$\frac{1}{c_0^2}\frac{\partial^2 p_\mathrm{a}}{\partial t^2} - \nabla \cdot \nabla p_\mathrm{a} = 0, \tag{6}$$

where p_a denotes the acoustic pressure.

2.5 Coupling between physical fields

To introduce the full coupling between the LinFlow PDE and the mechanics PDE, as well as the coupling between the LinFlow PDE and the acoustic PDE, we present the appropriate coupling conditions. The referenced coupling surfaces are defined in the next section in Fig. 1 and Fig. 2 and will be referenced in this section.

2.5.1 Coupling LinFlow-smooth-mechanics

The first case describes the coupling between LinFlow-, smooth-, and mechanics PDE. We choose an iterative approach and begin by calculating the smooth PDE. The solution of the smooth PDE (displacement and grid velocity) is then used in the integrators of the LinFlow PDE to calculate the flow of the air on the updated domain. Here we directly couple the velocity of the moving boundary of the

smooth PDE to the LinFlow PDE by applying the velocity as a Dirichlet boundary condition (BC) to the LinFlow PDE on the coupling surface Γ_{mech}. Afterward, the fluid stress tensor stemming from the LinFlow PDE is calculated, which is then applied to the mechanics PDE via

$$[\boldsymbol{\sigma}_{\mathrm{m}}] \cdot \boldsymbol{n}_{\mathrm{m}} = [\boldsymbol{\sigma}] \cdot \boldsymbol{n}_{\mathrm{m}} \quad \text{on } \Gamma_{\mathrm{mech}}, \tag{7}$$

where $\boldsymbol{n}_{\mathrm{m}}$ is the normal vector out of the mechanics domain. The object's deformation is calculated within the mechanics PDE based on this surface traction. Finally, the resulting displacement is used again as a Dirichlet BC for the smooth PDE, closing the coupling cycle.

2.5.2 *Coupling LinFlow-acoustics*

Finally, we couple the LinFlow PDE directly to the acoustic wave equation. This is done similarly to [9] via the continuity of surface traction

$$-p_{\mathrm{a}}\boldsymbol{n}_{\mathrm{f}} = [\boldsymbol{\sigma}] \cdot \boldsymbol{n}_{\mathrm{f}} \quad \text{on } \Gamma_{\mathrm{NC}} \tag{8}$$

as well as continuity of normal acceleration

$$\frac{\partial \boldsymbol{v}}{\partial t} \cdot \boldsymbol{n}_{\mathrm{f}} = -\frac{1}{\rho_0} \nabla p_{\mathrm{a}} \cdot \boldsymbol{n}_{\mathrm{f}} \quad \text{on } \Gamma_{\mathrm{NC}} \tag{9}$$

on the coupling interface Γ_{NC}. Here, $\boldsymbol{n}_{\mathrm{f}}$ denotes the normal vector facing out of the LinFlow domain. We also use non-conforming interfaces to reduce the overall degrees of freedom [13].

3. MODEL SETUP

For our investigations, we used a generic shutter with realistic geometry and material parameters. Due to the computational cost, we reduced the model to a 2D unit cell.

3.1 General

The definition of the geometry can be seen in Fig. 1 as well as Fig. 2. As it can be seen from Fig. 2 the mesh used in the LinFlow region (moving and stationary) is quite fine to resolve the boundary layers appropriately. Since we also vary the gap size within the parameter study, a minimum number of eight elements is guaranteed within the gap for all simulations. Overall, this results in roughly 43k degrees of freedom (DOF) for one simulation. Regarding the parameter study, we chose to vary the following parameters: pressure amplitude, gap size, and system stiffness (see Tab. 1). Overall, this results in 240 simulations. The material of the shutter as well as the air, is kept similar for all simulations. For the shutter, we use silicon for the material and for the air standard conditions at ambient pressure and 20° temperature. We assume that the deformation of the stator creating the narrow channel directly below the shutter is not significant and therefore

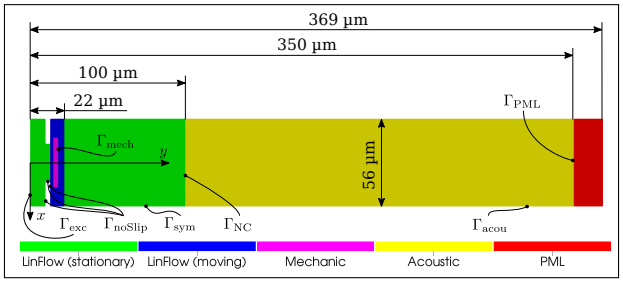

Figure 1: Model of the investigated shutter including geometrical properties.

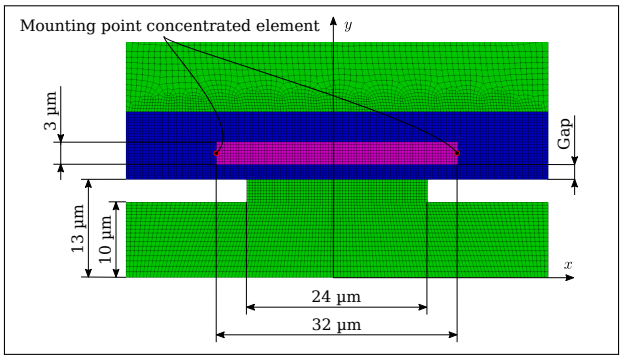

Figure 2: Close up of the model of the investigated shutter, including geometrical properties. The close-up also shows one example of the mesh used in the investigations.

Table 1: Definition of the parameter space.

Pressure amplitude		Gap	Stiffness
−50 Pa	50 Pa	1.0 µm	50 kN m^{-1}
−100 Pa	100 Pa	1.5 µm	100 kN m^{-1}
−200 Pa	200 Pa	2.0 µm	150 kN m^{-1}
−500 Pa	500 Pa	2.5 µm	200 kN m^{-1}
−1000 Pa	1000 Pa	3.0 µm	-
−2000 Pa	2000 Pa	-	-

do not model it.
The shutter itself is fixed in x-direction and can move in y-direction. On the left and right side of the shutter, a concentrated spring- and damping element are placed to simulate the mounting of the overall shutter. The damping is constant for all cases at $2\,\mathrm{mN\,s\,m^{-1}}$. This roughly corresponds to a Lehr's damping ratio of 0.0021 to 0.0042, depending on the parameters used, and ensures lower simulation time by ensuring a faster decay process. The artificially introduced damping ratio is relatively small and influences the shutter movement only minimally. An exemplary decay process can be seen in Fig. 3, which shows that the initial influence is minimal. Nevertheless, the decay process is damped out quicker, leading to a smaller rest amplitude of the oscillation and, therefore, a smaller evaluation error.

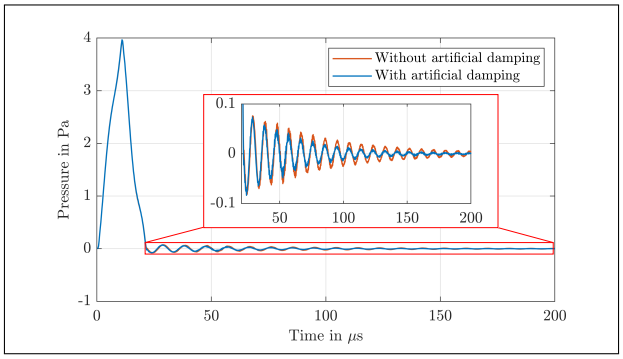

Figure 3: Exemplary comparison of the decay process at a measurement point located 200 µm from the coordinate origin in positive y-direction.

3.2 Boundary conditions and excitation

For the smooth PDE, we impose homogeneous Dirichlet BCs around its domain, which is denoted as LinFlow (moving). On the inside, a cut-out for the shutter is present where we use inhomogeneous Dirichlet BCs – the values for these BCs stem from the mechanics PDE. For the mechanics PDE, which is only computed on the region named accordingly, the movement is restricted in x-direction. Otherwise, we use the described coupling conditions and the concentrated elements to simulate the shutter motion. In the LinFlow domain, we use no-slip BCs at the interface Γ_{noSlip} and slip BCs at the interface Γ_{sym} to simulate the behavior of a unit cell. Besides the already mentioned couplings, we also excite the overall system in the LinFlow region on Γ_{exc} with a pressure pulse. Here we use a pressure pulse to accurately simulate an impinging wave – using a velocity excitation would result in a forced mass flow that does not reflect the actual application. Fig. 4 shows the normalized pressure pulse used for the excitation. This pressure pulse is triangular and has

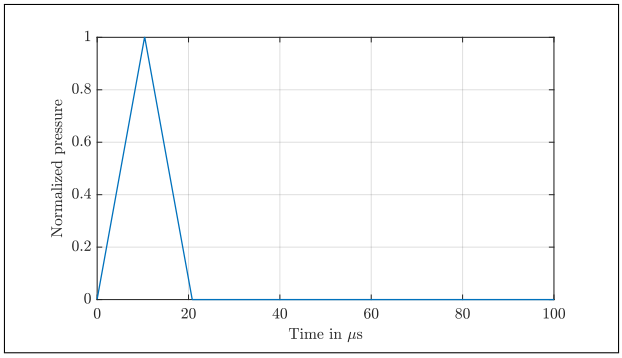

Figure 4: Normalized pressure pulse used for the excitation on Γ_{exc}.

a base frequency of 48 kHz, which corresponds to an input signal for an ultrasound pulse-based sound generation principle called Advanced Digital Sound Reconstruction (ADSR) [15]. This normalized pulse is scaled for the actual excitation with the pressure values given in Tab. 1. Based on this pulsatile excitation and the decay process, we choose a time step of 250 ns and a simulation time of 200 µs.

4. RESULTS

All simulations of the parameter study have been performed with the open-source finite element software *openCSF* [16].

4.1 Energy entering the system

For the analysis of the simulations, we evaluate the overall energy entering the system, the overall energy leakage through the shutter, and the transmitted energy. Here, we integrate the intensity I over a surface Γ and then again over the simulation time T_{sim} to get a scalar value for the energy E passing a surface. The first set of results given in Fig. 5 to Fig. 8 show the overall energy entering the system over the surface Γ_{exc} divided by the theoretical energy throughput of an unobstructed (open) channel. All results are shown for an overlap of 4 µm, representing the distance the shutter extends above the hole of the device.

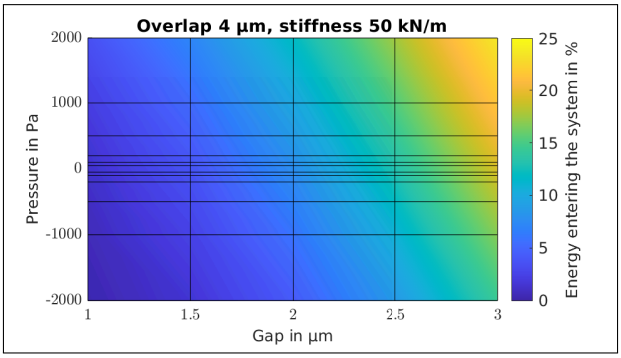

Figure 5: Energy entering the system over Γ_{exc} in percent of the case dependent maximum energy.

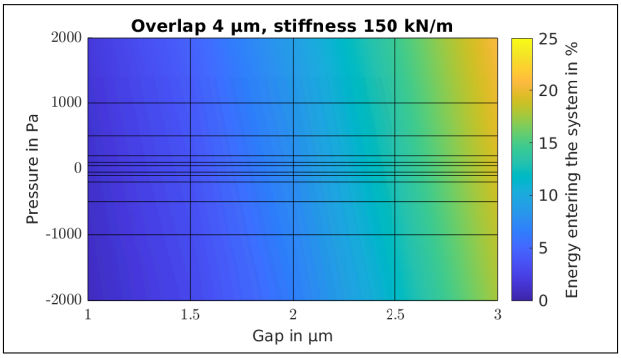

Figure 7: Energy entering the system over Γ_{exc} in percent of the case dependent maximum energy.

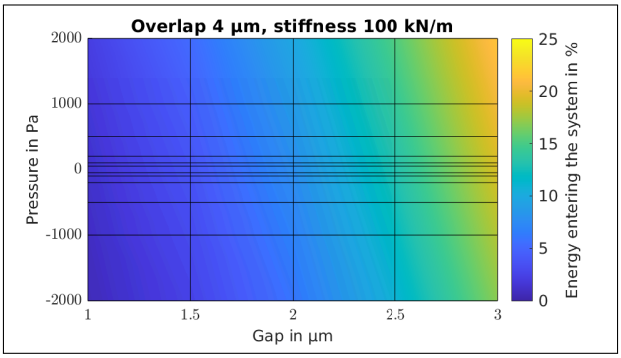

Figure 6: Energy entering the system over Γ_{exc} in percent of the case dependent maximum energy.

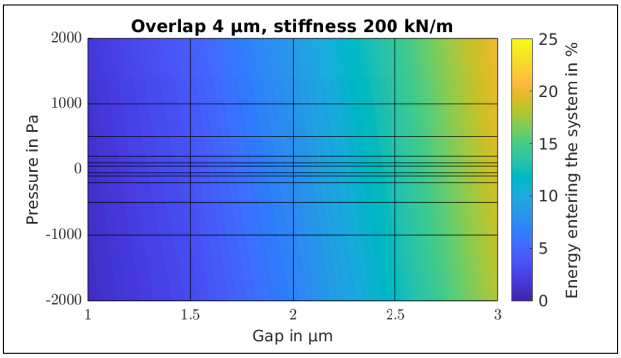

Figure 8: Energy entering the system over Γ_{exc} in percent of the case dependent maximum energy.

As shown in Fig. 5 to Fig. 8, the energy entering the system rises by increasing the gap as well as increasing the pressure amplitude. Since the energy passing through the shutter is divided by the theoretical maximum energy for this configuration, we see a drop in the energy with respect to the pressure axis. This is because the shutter gets pulled towards the stator for negative pressure configurations, which increases the sealing effect of the air gap. Since this effect does not occur when calculating the maximum energy, we see a drop for higher negative pressure values. Depending on the system's stiffness, the transducer's asymmetrical character is more pronounced. Especially for the lowest stiffness, we see a highly asymmetrical behavior of the energy entering the system. In the case of a damping application, this would lead to different efficiency depending on the sign of the impinging wave resulting in distortion and loss of effectiveness. The reason for the asymmetry, in general, is the movement of the shutter. Since the shutter will be pushed away, increasing the gap between the stator and the shutter, more air can pass through the gap. For a negative pressure, the effect is reversed, resulting in a smaller gap and less energy entering the system. Although the shutter gets pulled towards the stator, this does not lead to a collision between the two objects. When the shutter moves towards the stator, the effect of squeeze film damping hinders a collision even if the stiffness is small enough so that it would be possible by neglecting the damping effects [17]. Additionally, the shutter movement creates an inherent non-linearity since the position of the shutter, and therefore its damping properties for the impinging acoustic wave, is pressure dependent. From Fig. 5 to Fig. 8 it can be said that for damping applications, a very stiff shutter with a reasonably large gap is suitable. Depending on the absorption properties, the gap can be optimized. For a sealing application like in the case of ADSR, a smaller gap in combination with a

stiff shutter mount is preferable.

4.2 Transmitted energy

In the next step, the transmitted energy is analyzed. Therefore we evaluate the energy entering the system as well as the energy leaving the system. Dividing the energy leaving the system by the energy entering the system gives us a measure for the transmitted energy. The evaluation of the energy has been performed similarly to the last results where we integrate the intensity over the evaluation surfaces (Γ_{PML} and Γ_{Exc} in this case) and over time. The results are shown in Fig. 9 to Fig. 12. For the transmitted energy, similar statements as for the energy entering the system hold. One of the most significant differences can be seen by comparing Fig. 9 and Fig. 5. In Fig. 5, the lower left corner clearly shows the region with the lowest percentage of energy entering the system, whereas in Fig. 9, the corner shows higher transmitted energy than for example for lower pressure values. This is not the case when we go to higher values for the gap – here, we see a drop in the transmitted energy for increasing negative pressure amplitudes. For higher gap values, the asymmetry stems from the movement of the shutter, which seals the air channel better for increasing negative pressure values and vice versa. Below a critical gap size, this observation does not hold anymore, and the transmitted energy starts to rise again for increasing negative pressure amplitudes. The reason for this effect is the resulting squeeze film between the stator and shutter. The shutter does not move as much towards the stator for minimal gap values since the squeeze film drastically slows this movement. Hence, increasing the pressure amplitude (also for negative values) also increases the initial energy throughput.

Additionally, the percentage reflects the overall energy ratio, which is generally lower for the version where

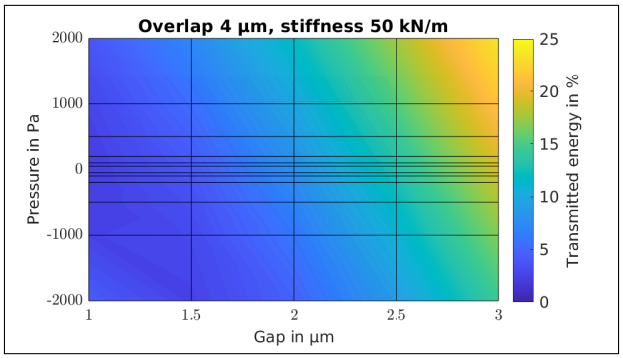

Figure 9: Energy transmitted through the system over Γ_{PML} in percent of the energy entering it.

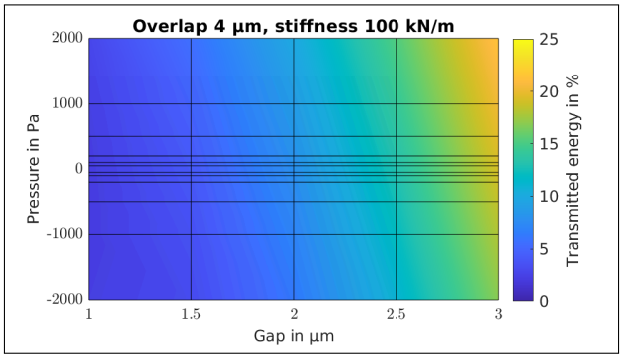

Figure 10: Energy transmitted through the system over Γ_{PML} in percent of the energy entering it.

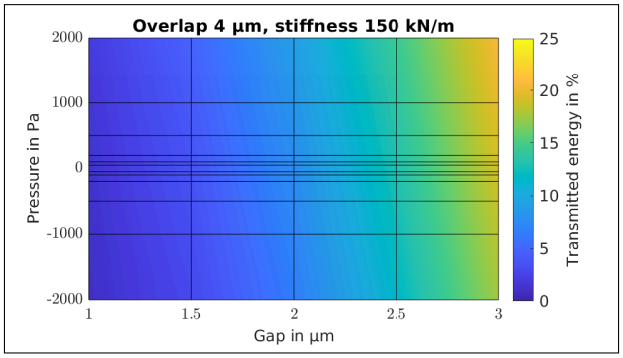

Figure 11: Energy transmitted through the system over Γ_{PML} in percent of the energy entering it.

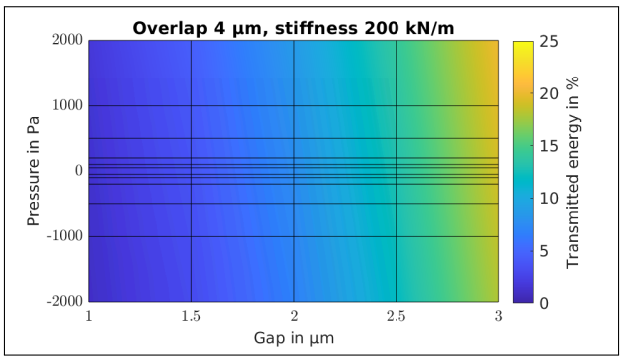

Figure 12: Energy transmitted through the system over Γ_{PML} in percent of the energy entering it.

the shutter gets pulled toward the stator. Hence, although the overall energy passed through the system is smaller, the ratio of transmitted energy to input energy increases even more than for positive pressure values. Furthermore, since this is a percentage of the maximum possible energy, this does not reflect the absolute value of the energy. When the pressure is higher, more energy can pass through the shutter, but pushing and pulling the shutter for positive and negative pressure values influences the symmetry heavily.

4.3 Leakage

Finally, we discuss the leakage energy getting transmitted through the shutter. The leakage energy is evaluated similarly as before by taking the energy flow over the interface Γ_{PLM} into account. The results can be seen in Fig. 13 to Fig. 16.

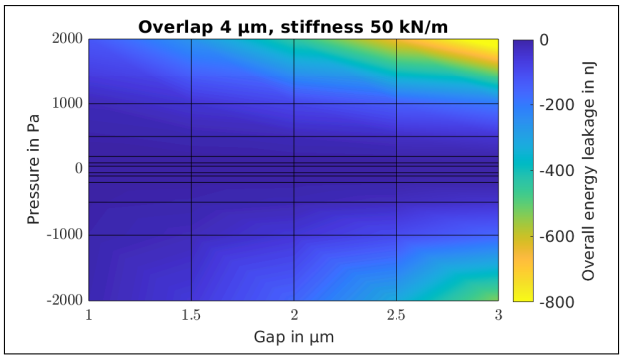

Figure 13: Energy transmitted through the system over Γ_{PML} (leakage energy).

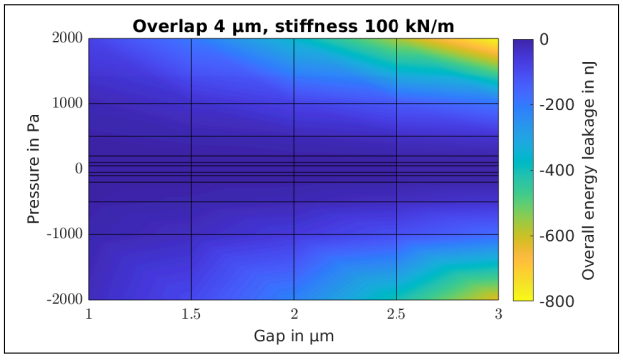

Figure 14: Energy transmitted through the system over Γ_{PML} (leakage energy).

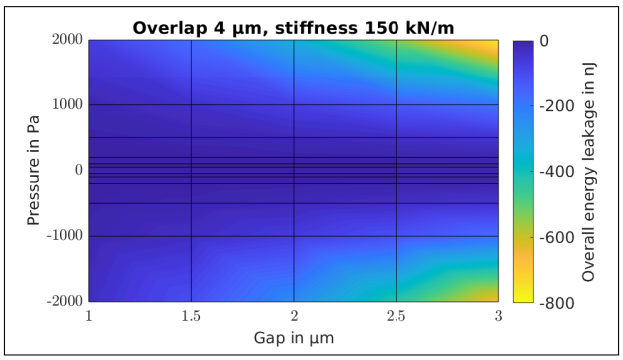

Figure 15: Energy transmitted through the system over Γ_{PML} (leakage energy).

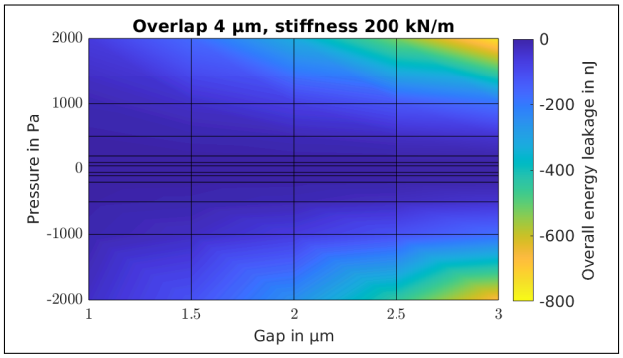

Figure 16: Energy transmitted through the system over Γ_{PML} (leakage energy).

As can be seen, the overall energy leakage rises throughout all gap sizes for increasing pressure amplitudes. Nevertheless, a similar asymmetrical behavior due to the shutter movement is seen throughout the results. The introduced non-linearity also affects the scaling property of the leakage energy with the sound pressure.

5. DISCUSSION

In this paper, we presented a unit cell of a shutter device which can be seen as an acoustic meta material. We analyzed the introduced model within a fully coupled multiphysics framework where we incorporated viscou-acoustic effects and the domain movement. Based on the results, we can see tendencies regarding the optimization for either damping applications (absorber) or sealing applications (shutter). For the absorber, the energy entering the system rises with the gap size, but so does the transmit-

ted energy (leakage energy). Furthermore, this effect will also be frequency dependent, which we did not discuss here. Hence, finding the optimal operation point is highly problem dependent. Nevertheless, increasing the stiffness and therefore reducing the asymmetry will help reduce undesired non-linearities due to pressure-dependent absorption characteristics. For sealing applications, the message is a lot clearer: Reducing the gap size and increasing the stiffness helps to reduce the leakage energy as well as asymmetrical and non-linear behavior, resulting in better system performance. For ADSR, this translates to optimizing the system to maximize the shutter stiffness and minimize the gap size. For a small gap size, pulsatile excitations pose a smaller problem than initially believed by the authors due to the strong damping effects of the squeeze film. This effect extends the operating range since contact between the stator and the shutter is less likely. Further research should be done to consider the influence of the overlap – which has not been varied in this study – as well as the influence of the gap size under consideration of slip boundary conditions taking molecular effects into account.

6. REFERENCES

[1] N.-T. Nguyen, X. Huang, and T. K. Chuan, "MEMS-Micropumps: A Review ," *Journal of Fluids Engineering*, vol. 124, pp. 384–392, 05 2002.

[2] D. Tumpold, M. Stark, N. Euler-Rolle, M. Kaltenbacher, and S. Jakubek, "Linearizing an electrostatically driven MEMS speaker by applying pre-distortion," *Sensors and Actuators A: Physical*, vol. 236, pp. 289–298, 2015.

[3] F. Stoppel, A. Männchen, F. Niekiel, D. Beer, T. Giese, and B. Wagner, "New integrated full-range mems speaker for in-ear applications," in *2018 IEEE Micro Electro Mechanical Systems (MEMS)*, pp. 1068–1071, 2018.

[4] H. Wang, Y. Ma, Q. Zheng, K. Cao, Y. Lu, and H. Xie, "Review of recent development of mems speakers," *Micromachines*, vol. 12, no. 10, 2021.

[5] B. Kaiser, H. A. G. Schenk, L. Ehrig, F. Wall, J. M. Monsalve, S. Langa, M. Stolz, A. Melnikov, H. Conrad, D. Schuffenhauer, and H. Schenk, "The push-pull principle: an electrostatic actuator concept for low distortion acoustic transducers," *Microsystems & Nanoengineering*, vol. 8, p. 125, 11 2022.

[6] A. Gemelli, M. Tambussi, S. Fusetto, A. Aprile, E. Moisello, E. Bonizzoni, and P. Malcovati, "Recent trends in structures and interfaces of mems transducers for audio applications: A review," vol. 14, no. 4.

[7] A. K. Au, H. Lai, B. R. Utela, and A. Folch, "Microvalves and micropumps for BioMEMS," *Micromachines*, vol. 2, pp. 179–220, 05 2011.

[8] T. Adachi *et al.*, "Mems microshutter array system for james webb space telescope," vol. 6687.

[9] D. Mayrhofer and M. Kaltenbacher, "Modeling and numerical simulations of mems shutter devices," in *WCCM-APCOM Congress 2022* (S. Koshizuka, ed.), Scipedia S.L., 2022.

[10] H. Hassanpour Guilvaiee, F. Toth, and M. Kaltenbacher, "Fem-modeling of thermal and viscous effects in piezoelectric mems loudspeakers," *PAMM*, vol. 22, no. 1, p. e202200027, 2023.

[11] A. Kierkegaard, S. Boij, and G. Efraimsson, "A frequency domain linearized navier–stokes equations approach to acoustic propagation in flow ducts with sharp edges," *The Journal of the Acoustical Society of America*, vol. 127, no. 2, pp. 710–719, 2010.

[12] D. Mayrhofer, K. Ropppert, and M. Kaltenbacher, "A moving mesh method for fluid-solid-acoustic," *Unpublished manuscript*.

[13] M. Kaltenbacher, *Numerical Simulation of Mechatronic Sensors and Actuators: Finite Elements for Computational Multiphysics*. Springer, 3rd ed., 2015.

[14] G. Link, M. Kaltenbacher, M. Breuer, and M. Döllinger, "A 2d finite-element scheme for fluid–solid–acoustic interactions and its application to human phonation," *Computer Methods in Applied Mechanics and Engineering*, vol. 198, no. 41, pp. 3321–3334, 2009.

[15] D. Mayrhofer and M. Kaltenbacher, "A new method for sound generation based on digital sound reconstruction," *Journal of Theoretical and Computational Acoustics*, vol. 29, p. 2150021, 12 2021.

[16] M. Kaltenbacher, "openCFS." `https://www.opencfs.org`, 2023.

[17] M. Bao, H. Yang, Y. Sun, and Y. Wang, "Squeeze-film air damping of thick hole-plate," *Sensors and Actuators A: Physical*, vol. 108, pp. 212–217, 11 2003.